The Ocean Response to Low-Frequency Interannual Atmospheric Variability in the Mediterranean Sea. Part II: Empirical Orthogonal Functions Analysis

G. KORRES

Laboratory of Meteorology, Department of Applied Physics, University of Athens, Athens, Greece

N. PINARDI

Istituto di Scienze dell'Atmosfera e dell'Oceano, CNR, Bologna, Italy

A. LASCARATOS

Laboratory of Meteorology, Department of Applied Physics, University of Athens, Athens, Greece

(Manuscript received 18 March 1999, in final form 13 April 1999)

ABSTRACT

This paper deals with the statistical analysis of the nine years of model simulation described in Part I. Here the focus is on different applications of EOF analysis in the time domain, pointing out the spatial–temporal scales of the Mediterranean general circulation variability. The analysis is carried out either in 2D or 3D space and is based on the singular value decomposition technique. Seasonal and interannual variability of the Mediterranean Basin occur on the subbasin gyre spatial scales. Two major events of interannual variability occurring during the winters of 1981 and 1986 are identified through the analysis of the barotropic/baroclinic circulation. Barotropic streamfunction EOF analysis shows that after strong winter wind anomaly events, which enhance cyclonic circulation, the basin relaxes to opposite sign vorticity regimes. The analysis confirms that the largest barotropic anomalies are locked to the winter season.

The temperature 3D EOF analysis highlights that three vertical amplitude modes can represent all the variance in the upper 400 m of the water column. The second mode, which has basin-wide scales with meridional gradients, is surface intensified and contains the seasonal cycle anomalies. The surface ocean signal propagates into the mixed layer within a period of three months.

The dynamic height field interannual variability is pronounced at the subbasin-scale gyres and it shows anomalies in summer of 1981 and 1986, six months after the winter forcing anomaly events.

The study of the correlation between surface heat fluxes and SST variability (extended EOF) shows that winter anomalous cooling events (1981, 1987) can generate different effects on the SST response involving both large-scale advection/diffusion processes and subduction events.

1. Introduction

The empirical orthogonal function (EOF) analysis method has been extensively used in meteorological studies since the first time it was introduced by Lorenz (Lorenz 1956). In oceanography its use in studying GCM results is quite new but we think very promising.

The EOF technique is a multivariate analysis designed to derive the dominant variability patterns from a set of fields of any type. The EOF patterns are the eigenvectors of a covariance matrix, so in this sense they constitute an important property of the probability distribution of the variables themselves. These eigenmodes are characterized by several useful properties such as mutual orthogonality and efficient representation of the initial field (reduction of the problem's dimensionality).

North (1984) has shown that under certain circumstances the dynamical modes of a mechanical system can coincide with its EOFs. These circumstances are however very special cases that require that the system is governed by a normal operator. In most real-world cases, however, dynamical processes are interrelated and not orthogonal to each other so such a symmetry between EOFs and dynamical modes cannot exist. Recently, in the context of dynamical models, Navarra (1993) shed light on the relationship between the EOF modes and the growing dynamical modes of the linearized initial value problem related to the fully nonlinear primitive equations system. In the meteorological literature one can trace a variety of applications of this

Corresponding author address: Dr. Nadia Pinardi, SAO–CNR, Via Gobetti 101, 40129 Bologna, Italy.
E-mail: n.pinardi@isao.bo.cnr.it

technique. Extended EOF (EEOF) and canonical correlation analysis have been used and intercompared by Wallace et al. (1991), for analyzing the relationships between two meteorological fields. Fukumori and Wunsch (1991), on the other hand, introduce the singular value decomposition (SVD) method for the study of different tracer fields in the Atlantic Ocean system.

In this paper we assess the temporal and spatial scales of the Mediterranean general circulation seasonal and interannual variability through the statistical analysis of a 9-yr GCM simulation described in (Korres et al. 2000, hereafter referred to as Part I). In that paper we present a description of the model central interannual experiment (1980–89) along with a detailed discussion of the results. We have already seen the structure of the subbasin-scale features that determine the general circulation flow field at the overall basin scale. We have also pointed out that interannual atmospheric forcing is responsible for major changes in the circulation in several areas of the basin. The somewhat limited duration of the model integration sets some limits on the assessments of long timescale circulation variability in the Mediterranean. However we were able to extract statistically significant signals.

In appendix A we give a brief description of the basic principles behind 2D/3D EOF and EEOF analysis methods. In section 2 we introduce the formalism and method to analyze the model fields. Section 3 deals with the data preprocessing. In section 4 we offer a discussion of the results obtained from the statistical analysis and the paper concludes with section 5 where we summarize the main findings.

2. Methodology

In appendix A some of the fundamentals of ''classical'' EOF analysis (Preisendorfer 1988) are given showing at the same time the equivalence of EOF and the SVD method (Golub and van Loan 1989).

Let us indicate by $\phi_j(x)$ a time series of 2D fields (e.g., the barotropic streamfunction) from the model simulation, where $x = 1, \ldots, p$ indicates the number of horizontal grid points and $j = 1, \ldots, n$ the number of time steps recorded. Thus our time series contains n realizations at each x point and we can write $\mathbf{D}$ as the matrix:

$$\mathbf{D} = \begin{pmatrix} \phi_1(x_1) & \cdots & \phi_n(x_1) \\ \vdots & & \\ \vdots & & \\ \phi_1(x_p) & \cdots & \phi_n(x_p) \end{pmatrix} \tag{1}$$

or $d(x, t)$ the corresponding field containing the n realizations of $\phi_j(x)$. Following the procedure outlined in appendix A we can write

$$d(x, t) = \sum_{i=1}^{r} e_i(x)\lambda_i^{1/2} a_i(t), \tag{2}$$

where e_i are the EOF patterns, λ_i the EOF eigenvalues, and a_i the amplitude time series (ATS) of each EOF mode.

Let us now indicate by $\phi_j(x, z)$ the time series of a 3D field from the model simulation (e.g., temperature field at various depths) with $x = 1, \ldots, p$ indicating again the number of horizontal grid points; $z = 1, \ldots, m$ the number of levels in the vertical; and $j = 1, \ldots, n$ the number of time realizations. In addition, $\mathbf{D}$ is now the $nm \times p$ block matrix,

$$\mathbf{D} = |\mathbf{W}(1) \cdots \mathbf{W}(n)|^{\mathrm{T}}, \tag{3}$$

where $\mathbf{W}(t)$ is the $p \times m$ local matrix representing the 3D field at a specific time t ($t = 1, \ldots, n$):

$$\mathbf{W}(t) = \begin{pmatrix} \phi_1(x_1, z_1) & \cdots & \phi_n(x_1, z_m) \\ \vdots & & \\ \vdots & & \\ \phi_1(x_p, z_1) & \cdots & \phi_n(x_p, z_m) \end{pmatrix}$$

Following decomposition type I described in appendix A we can represent field $d(x, z, t)$ as

$$d(x, z, t) = \sum_{i=1}^{r} e_i(x)\sigma_i a_i(z, t), \tag{4}$$

where e_i are the (depth invariant) EOF patterns, σ_i the EOF singular values (the square root of EOF eigenvalues), and a_i' the ATS of each EOF mode. In this type of analysis the ATSs vary also with depth.

Following decomposition type II (described also in appendix A) the field $d(x, z, t)$ can be alternatively decomposed as

$$d(x, z, t) = \sum_{i=1}^{r'} e_i'(x, z)\sigma_i' a_i'(t), \tag{5}$$

where e_i' are the 3D EOF patterns, σ_i' the EOF singular values, and a_i' the ATS of each EOF mode.

Finally, let us assume that m in (3) indicates different (heterogeneous) 2D physical fields instead of different levels in vertical. In this case the EOF analysis is called extended EOF and can be done with decomposition types I or II. In our application of EEOF we use decomposition type I in order to analyze the temporal relationship between the total heat flux and the model SST fields.

3. Data preprocessing

In the previous section (and in appendix A) we have presented the method and formalism of EOF analysis without referring to the data normalization procedure. It is possible to extract the EOF modes from the raw (nonnormalized) dataset but this approach can suffer from many problems. For example applying the analysis on a heterogeneous set of data that involves different physical units, the first EOF modes will concentrate on the field with the larger values. Thus, a long series of

modes will be needed in order to represent the original fields. The explanation for this behavior lies in the fact that the EOF analysis is a scatter-oriented method. Thus, we decided to standardize all the different entries of the matrix **D** in (1) by subtracting the steady-state mean $\overline{\phi}(x)$ of each gridpoint time series,

$$\overline{\phi}(x) = \frac{1}{n} \sum_t \phi_t(x),$$

and dividing by the associated standard deviation,

$$\text{std dev}(x) = \left(\frac{1}{n-1} \sum_t [\phi_t(x) - \overline{\phi}(x)]^2 \right)^{1/2}.$$

This normalization is used for 2D EOF analysis, EEOF, and the 3D EOF decomposition of type-II form.

In the 3D EOF decomposition type I, which involves a separation of the spatial horizontal patterns from the vertically varying amplitude time series, normalization was performed on a level basis; all the gridpoint time series at depth z_k were differenced with respect to a level steady-state value,

$$\overline{\phi}(z_k) = \frac{1}{n \cdot p} \sum_x \sum_t d(x, z_k, t),$$

and then divided by the level standard deviation,

$$\text{std dev}(z_k) = \left(\frac{1}{n \cdot p - 1} \sum_x \sum_t [\phi(x, z_k, t) - \overline{\phi}(z_k)]^2 \right)^{1/2}.$$

This was done in order to give the same weight to all levels entering the analysis, thus avoiding the situation where the first modes represent the upper high variance levels while the higher modes explain the behavior of deep (low variance) levels. However our choice of levels entering the analysis emphasizes the upper-ocean variability.

Another issue concerns the seasonal cycle contained in each time series producing cyclostationary character. In order to eliminate the seasonal cycle we form the so-called anomaly fields by subtracting an estimated monthly mean climatology from the original data. We have used the seasonal climatology estimated from the nine years of model integration. Additionally, a six-point Lanczos low-pass filter was applied to each time series in order to eliminate higher frequencies that can remain in the anomaly fields.

All the fields analyzed are evenly distributed horizontally on the ¼° × ¼° model grid. In the 3D EOF analysis (decomposition types I and II) only the grid points that extend to the deepest level are considered. The temperature and dynamic height 3D fields appear to be smooth enough; thus, no spatial filtering before the analysis is needed. In the case of 2D EOF analysis of the barotropic streamfunction fields, a simple five-point spatial smoother is used to eliminate small-scale noise. The time sampling in all cases is one month (monthly means). Finally, before all types of analyses, a linear trend in time is estimated and subtracted from each separate time series.

4. Results from statistical analysis

a. Barotropic streamfunction analysis

We investigate first the dominant time and space scales of the barotropic streamfunction fields. As a first step we apply the analysis to the total fields knowing that most of the variance will be concentrated on the seasonal cycle.

The amplitude time series associated with the first and second modes are shown in the left column of Fig. 1, while in Fig. 2a we show the spatial patterns of the same two modes. Note that the spatial patterns are scaled in such a way that the value at each grid point is exactly the correlation coefficient between the associated ATS and the original normalized time series at this point. Areas that involve mode amplitude higher than 0.6 have been lightly shaded in order to better show the peaks of variability in the field. The first two modes contain 48% of the total variance, with the first mode (which represents the seasonal cycle) containing 35%. Spectral analysis of the ATS time series shows the existence of periodicities of 1.7, 5.3 (first ATS), and 2.6 yr (second ATS), which, however, correspond to a much lower spectral energy. We should mention here that due to the short length of the time series analyzed, low-frequency spectral peaks (e.g., 5.3-yr periodicity) have no statistical significance. The ATS time series exhibit peaks of variability during the winters of 1981 and 1986, which correspond to strong wind curl anomaly events occurring during those periods (see Part I and below). We note also that the second ATS is lagging the first one by three months.

The spatial pattern of the first EOF (Fig. 2a) is characterized by large scales with enhanced amplitudes on the subbasin scale. It involves an in-phase oscillation of the whole basin around the steady-state mean, with the exceptions being the center located at the Sicily Straits, and the southern Ionian area, which oscillates out of phase with the rest of the basin. The second spatial pattern is dominated by smaller scales in the western Mediterranean (WMED), whereas the center of maximum variability lies in the southern Ionian. For this mode the WMED oscillates out of phase with respect to the most of the eastern Mediterranean (EMED). The eastern basin involves two out of phase oscillators, with one of them encompassing most of the Levantine Basin.

The same type of analysis was applied to the anomaly barotropic streamfunction fields and it is shown in Figs. 1b and d and 2b. For the removal of high-frequency signal from the anomaly fields, an additional six-point Lanczos filtering procedure was applied to the anomaly fields as already discussed in section 3.

The first two modes of the analysis represent now 50% of the overall variability. The first ATS is char-

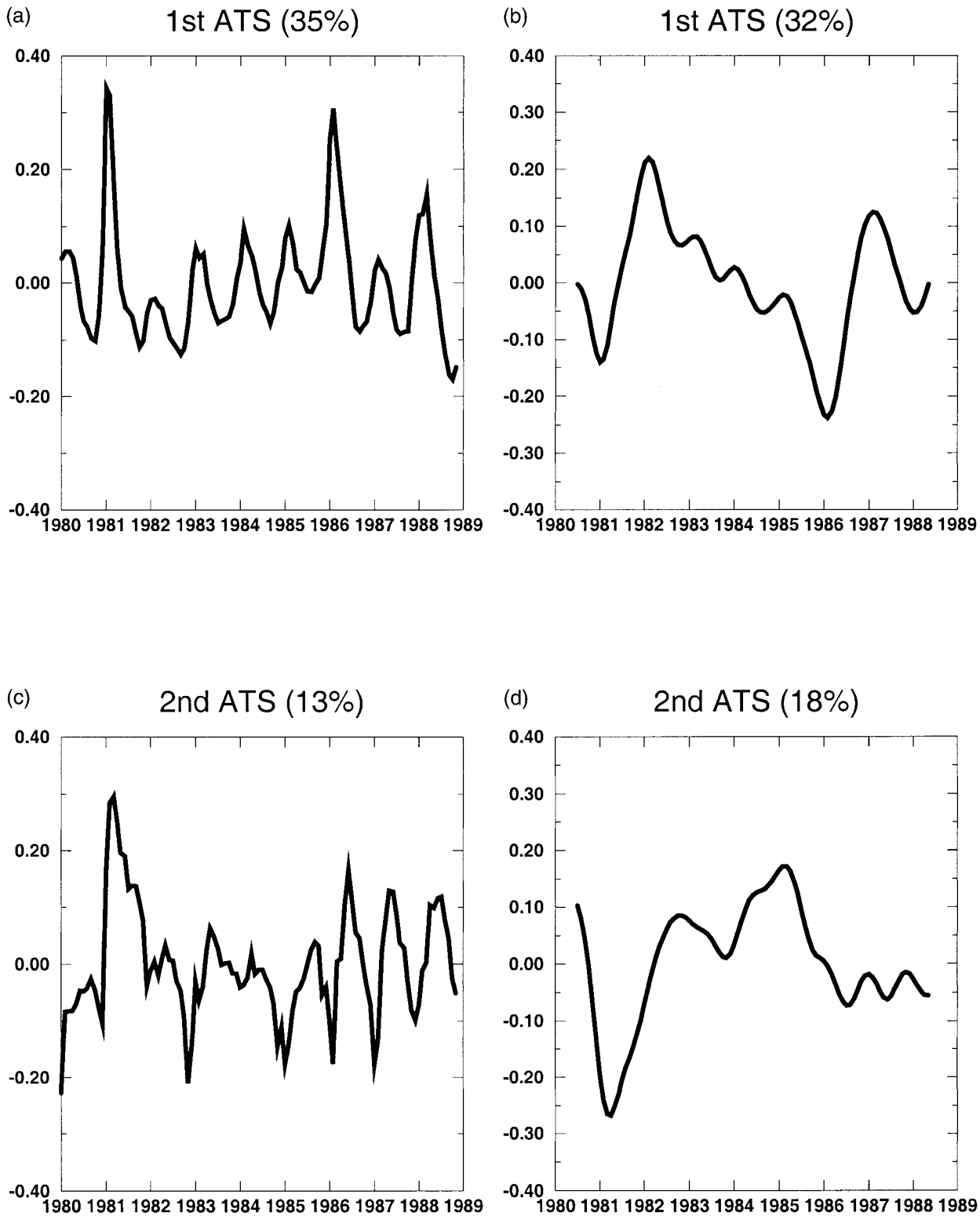

FIG. 1. (a) and (c) The first two amplitude time series of the 2D EOF analysis applied on the total barotropic streamfunction field. (b) and (d) The corresponding ATSs for the anomaly barotropic streamfunction field analysis are shown.

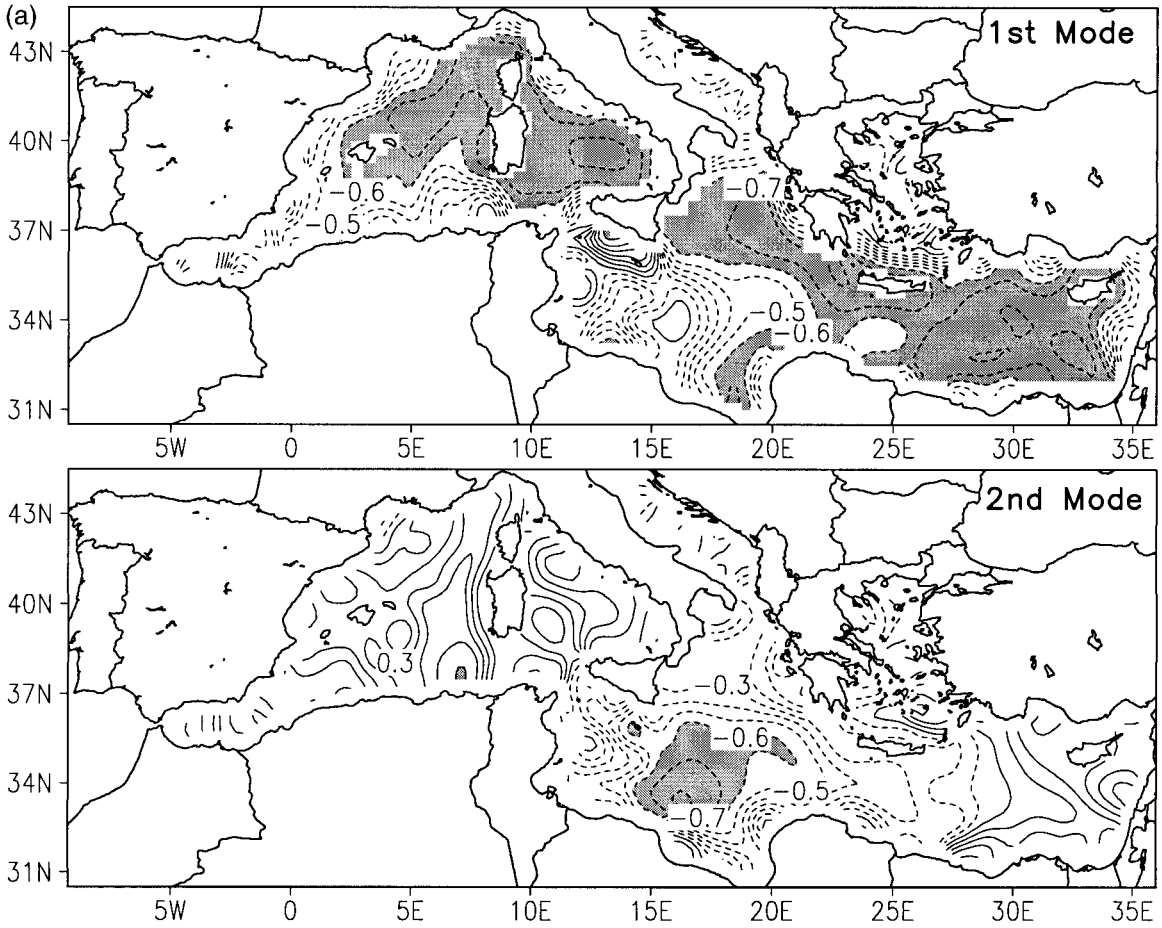

FIG. 2. (a) The first two EOF patterns corresponding to the total barotropic streamfunction field. (b) As in (a) but for the anomaly barotropic streamfunction field.

acterized by spectral peaks at 5.3 and 2.6 yr. This anomaly amplitude time series shows the large signal of the winters of 1981 and 1986 during which the cyclonic vorticity input from the wind field is high and the barotropic circulation intensified strongly.

In Fig. 3 we show the January climatology of the wind stress curl along with the anomalies of years 1981 and 1986. The winter of 1981 involves a very pronounced increase of cyclonic vorticity input for most of the EMED with maxima in the central Ionian Basin. On the other hand during the winter of 1986 the cyclonic vorticity intensification is less than the winter of 1981 and affects most of the Mediterranean Basin with maxima within the WMED. After winter years of this kind, the ATSs show a transition to an opposite circulation direction state or a weakening of the cyclone dominated regime of the previous winter. Inspection of the spatial pattern associated with the first mode (Fig. 2b) shows intensification in the Levantine, the north-central Ionian, the eastern Tyrrhenian, and the Balearic Islands area. The pattern of the first anomaly EOF is characterized by subbasin gyres and even smaller scales. The second mode (accounting for 18% of the total variance) captures a 5.3-yr cycle that, however, is not well resolved by the 9-yr record available. Its spatial pattern resembles the second mode of the total barotropic streamfunction fields analysis, since the center of maximum amplitude occurs in the southern Ionian Basin. Inspection of the ATS associated with the second anomaly mode shows a strong intensification during the winter of 1981. Overall, ATSs of both modes demonstrate that the interannual variability is locked to the seasonal cycle since in most cases the amplitude time series intensifies during early winter months (January–February). In both types of analysis (with or without the seasonal cycle removed), the statistical significance of the modes obtained was tested using a Monte Carlo technique (Preisendorfer et al. 1981) designed to draw the 95% and 5% confidence levels for each mode. In appendix B we discuss this procedure. All modes examined here proved to be significant above the 95% significance level.

b. EOF analysis of temperature and dynamic height fields

This section deals with the 3D EOF analyses performed on the temperature and dynamic height fields at

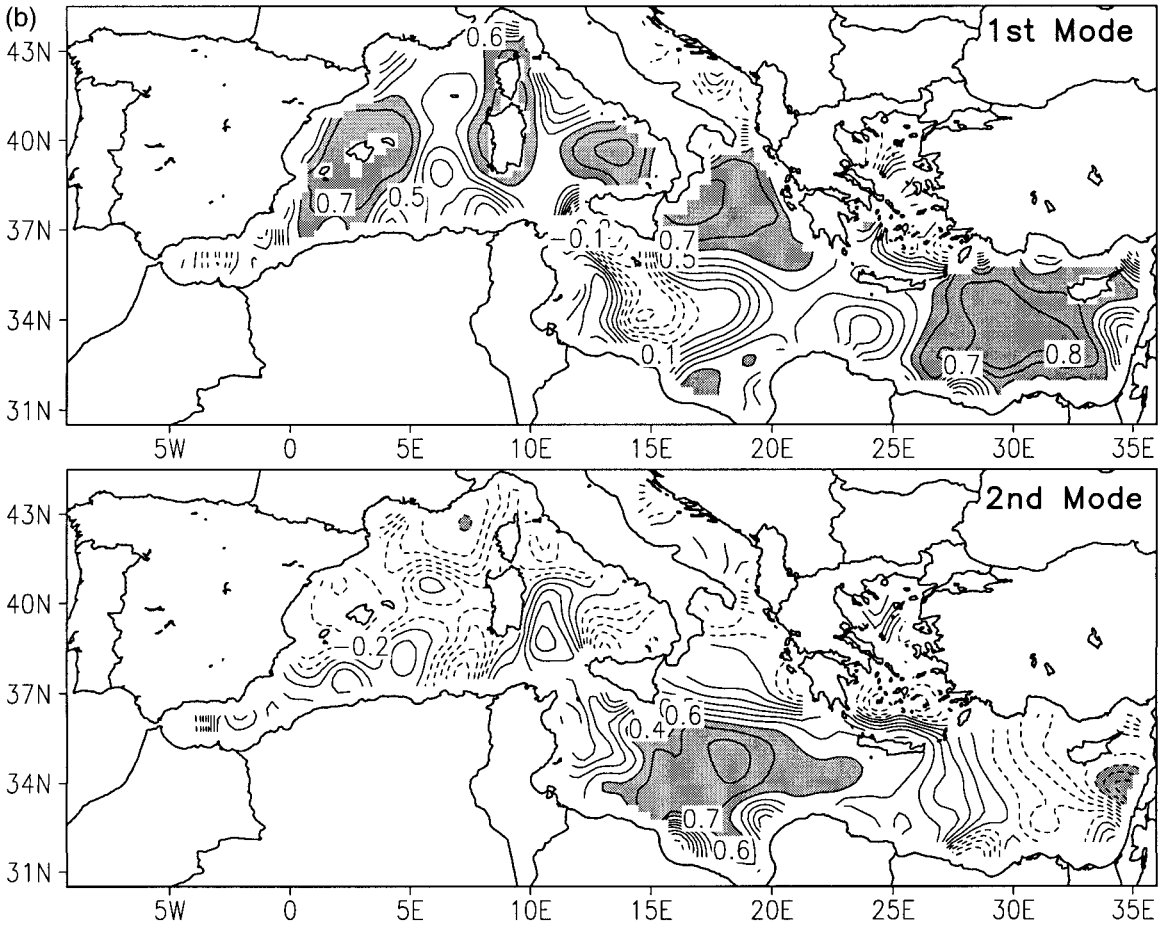

FIG. 2. (*Continued*)

depths of 5, 15, 30, 50, 80, 120, 160, 200, 240, 280, 340, 420, 500, 620, and 850 m. For the dynamic height fields calculation, a reference level at 1000 m was used. The analyses were done with decomposition types I and II described in section 2 (and in appendix A). The analyses with decomposition type I were applied to the total temperature fields (i.e., seasonal cycle included) and to the dynamic height anomaly fields as well. Prior to the analyses, the model output data at each depth were normalized by subtracting the spatial steady-state mean and dividing by the associated standard deviation as explained in section 3. The decomposition type-II analysis was applied only to the anomaly dynamic height fields. In both types of analyses, grid points shallower than 850 m (i.e., $z < 850$ m), for temperature, or 1000 m (i.e., $z < 1000$ m), for dynamic height fields, were excluded.

We present first the results of decomposition type I applied on the total temperature field. In Fig. 4 we show the ATSs [$a_1(z, t)$, $a_2(z, t)$, and $a_3(z, t)$] at depths of 5, 120, 240, and 420 m. The spatial patterns associated with the first, second, and third modes account for 64%, 25%, and 4% of the normalized temperature second moments and they are shown in Fig. 5. The fraction of total scatter accounted for by the first three modes and the fraction of residual scatter accounted for by modes 2 and 3 are shown in Figs. 6a and 6b, respectively.

Comparison of the first mode spatial pattern with the overall mean (in time and depth) temperature field (not shown) demonstrates that the first mode describes the overall mean and $a_1(z, t)$ its temporal variability. This mode accounts for most of the total second moments below 100 m. Its spatial pattern is a dipole (eastern and western basins out of phase) due to the fact that the WMED is on average colder than the EMED. A prominent feature of this pattern (of the overall mean as well) is its large zonal gradients near the eastern boundaries of the continents and islands. This mode is clearly related to the overall heat content of the basin, which shows both seasonal and interannual time frequencies.

The spatial pattern associated with the second mode describes an in-phase oscillation of the whole basin having a zonal character in most of the Mediterranean Basin area involving a positive southward gradient in the central Balearic, the central Ionian, and the easternmost Levantine areas. This second mode is the dominant one in the first 100 m and represents the seasonal cycle of the upper temperature levels (with a minimum during

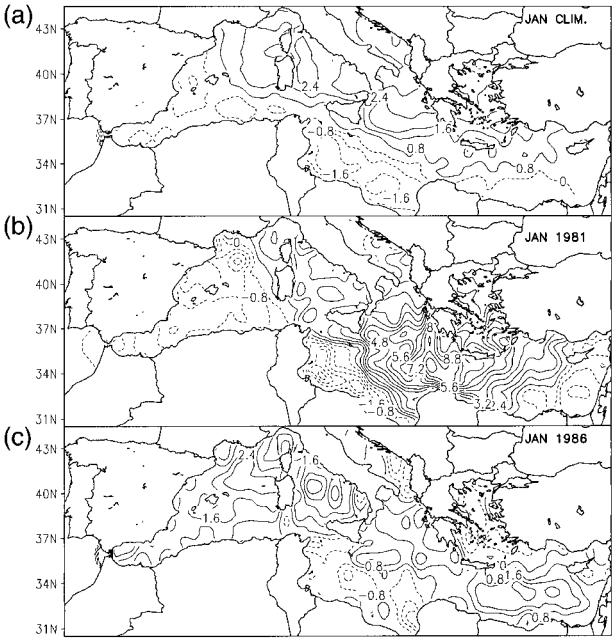

FIG. 3. January climatology of (a) wind stress curl field and (b) wind stress curl anomaly for Jan 1981 and (c) Jan 1986. The units are 10^{-8} dyn cm^{3}.

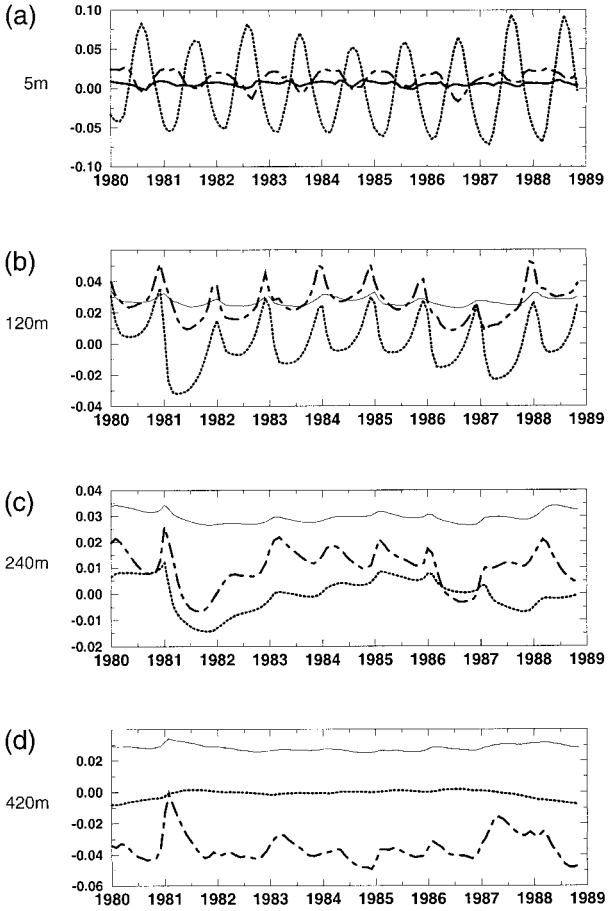

FIG. 4. The ATS corresponding to the first three modes of decomposition type I applied to the temperature fields, at the depths of 5, 120, 240, and 420 m. Continuous line corresponds to the first mode; dotted and dashed lines to the second and third modes, respectively.

early winter and a maximum during summer), as can be deduced from the $a_2(z, t)$ coefficients (shown in Fig. 7) in the upper mixed layer levels. There are also interannual positive peaks of variability (decreasing in magnitude with depth) superimposed on the seasonal cycle—the most important occurring during the summers of 1987 and 1988, implying a net heating of the upper layers. Inspection of the time series in Fig. 7 reveals that on the seasonal timescale, temperature variations propagate downward from the surface down to 80 m within a 3–4-month period during summer, while during winter this interval is reduced to 1–2 months. The effects of the winter 1981 strong cooling (see Fig. 8 for the heat flux anomaly field) are evident at a depth of 50 m. The mode gradually loses its seasonal character with depth.

Two important interannual variations emerge during the winters of 1981 and 1987 at a depth of 120 m, involving a temperature decrease for the whole basin (Fig. 4). At 240 m these anomalies are more prolonged in time and involve the summer period of 1981 and 1987 as well. Note also that the winter 1981 anomaly is more pronounced. This is probably due to the combined effect of wind and heat flux anomalies occurring during that period. As shown in Figs. 8 and 9 the winter of 1981 involves very significant anomalies for both the heat flux and wind stress fields.

The third mode accounts for a considerable fraction of the residual scatter between 400 and 600 m and is of some importance between 100 and 200 m (see Fig. 6). At these depths the behavior of the third ATS resembles the second mode while deeper than 400 m it is the mode accounting for the largest fraction of total variance. Furthermore, we can call this mode the Levantine Intermediate Water (LIW) mode for temperature, since 400 m is the depth at which LIW occurs in the model. The third mode contains smaller spatial scales of variability compared to the first two modes and has a pronounced boundary-intensified character.

We now investigate the structure of the dynamic height fields by applying decomposition types I and II to the total fields with only the steady-state components removed. The decompositions were also applied to the anomaly fields (i.e., seasonal cycle subtracted). The use of both decompositions allows us to investigate the different structures of seasonal and interannual signals in the baroclinic flow field.

We focus the discussion on the first two modes of decomposition type I, which contain 26% and 18% of the total scatter, respectively. The spatial patterns are shown in Fig. 10, while in Fig. 11 we present the coefficients $a_1(z, t)$ and $a_2(z, t)$ at all the analysis levels. Note that the dynamic height modes behave similarly at all levels as functions of time. The first mode involves

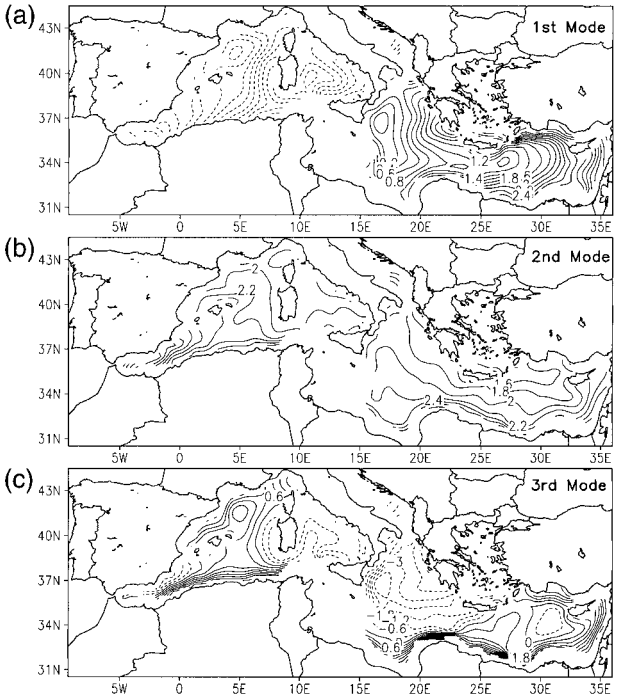

FIG. 5. The spatial patterns corresponding to the first three modes of decomposition type I applied to the temperature fields.

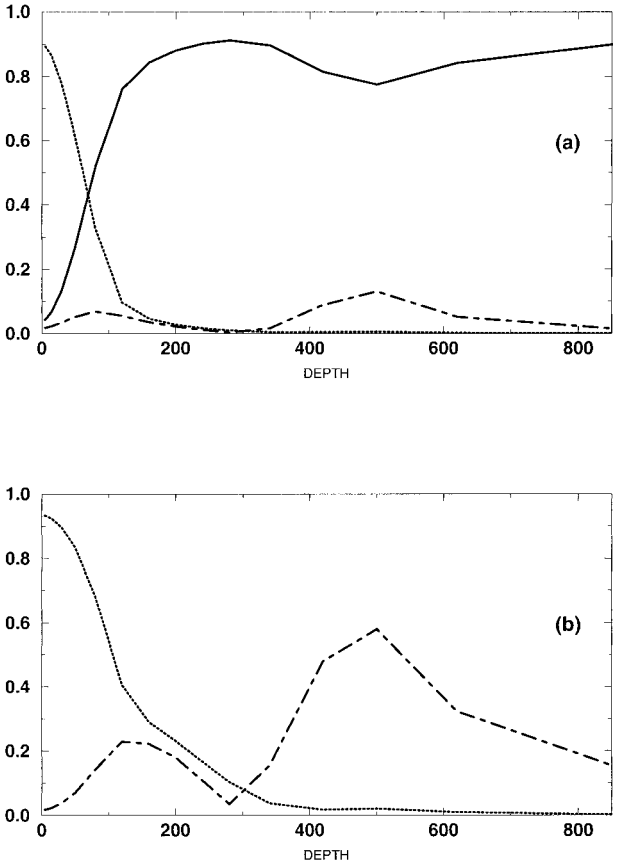

FIG. 6. (a) Percentage of total scatter accounted by the first (continuous line), second (dotted line), and third (dashed line) modes as a function of depth. (b) Percentage of residual scatter accounted by the second (dotted line) and third (dashed line) modes of the same analysis as a function of depth.

two important peaks of variability occurring during the years 1981 and 1986 (Fig. 11). The 1981 peak is centered at the beginning of summer 1981 and thus we can speculate that it describes a delayed response to the winter 1981 external forcing anomaly (shown in Figs. 8 and 9). The 1986 peak is instead synchronous with the forcing anomaly of winter 1986 (shown also in Figs. 8 and 9). Both 1981 and 1986 events have an average duration of 4–5 months and they become less pronounced with depth. The years between the two big events that were identified involve no significant variability of the baroclinic circulation.

The spatial pattern associated with the first mode is dominated by subbasin gyre scales and concentrates mainly in the central-eastern Levantine (encompassing the Rhodes gyre) and the central Tyrrhenian areas. On the other hand, the spatial pattern associated with the second mode intensifies clearly in the central Ionian, the central Balearic, and the Provencal–Catalan Basins. It is interesting to note the existence of a structure within the eastern Levantine Basin resembling the Mersha–Matruh gyre.

We proceed now to the analysis of decomposition type II applied on the dynamic height anomalies. The first two dominant modes of the analysis contain 45% (24% for the first and 21% the second) of the total variance. The EOF patterns $e_1(x, z)$ and $e_2(x, z)$ at various depths are shown in Figs. 12 and 13, respectively. The first noticeable feature of these patterns is their rather uniform character in the vertical. Different scales of variability are described by each of these two modes, but in both of them there is significant variability at the subbasin gyre scales. The first mode involves maxima localized in the Rhodes gyre area, along the western coasts of Corsica and Sardinia (an area where the northward flow of modified LIW occurs), within the Tyrrhenian Basin, and along the Spanish continental shelf. The EOF pattern associated with the second mode (Fig. 13) is strongly intensified in the central Ionian Basin, in the central part of the Tyrrhenian Basin, and in the eastern Levantine Basin.

The amplitude time series $a_1(t)$ and $a_2(t)$ are shown in Fig. 14. The first ATS is characterized by an anomalous amplitude change in 1986 and 1987. The first ATS shows a negative extreme is achieved during the winter of 1986 and a positive one during the summer period of 1987. On the other hand, the second ATS involves two negative extrema occurring during the late winter of 1981 and in the midwinter of 1986, respectively. Since the first mode is associated with the Rhodes gyre amplitudes and LIW pathways, it is possible to argue that relevant changes in LIW structure occurred during

1986 and 1987. The anomalous forcing and response in 1981 did not generate changes in LIW. This is the second ATS time series (Fig. 14) that is amplified in the Ionian Basin and not in the Rhodes gyre area.

By comparing the results of decomposition types I and II on the anomaly dynamic height fields, we can conclude that both analyses involve the same temporal–spatial scales of variability, and the same geographical center locations of variability extrema. However the type-II analysis allowed us to distinguish between the winter events of 1981 and 1986. In fact, the first produced an anomaly in the Ionian Basin baroclinic structure, while the second involved changes in both LIW and Ionian baroclinic general circulation structures.

c. *On the temporal relationship between heat fluxes and SST fields*

We analyze here the common modes of behavior of Q_T and SST fields, through the EEOF analysis explained in appendix A. The interative scheme of the model for the computation of the total heat flux Q_T at each time step (see Part I) allows a one-way feedback between the ocean and the atmosphere (the air temperatures and relative humidity are fixed). Our SST is the model first level temperature field (denoted by T_k). The equation for T_k is

$$\frac{DT_k}{Dt} = \frac{Q_T}{\rho C_p \Delta z_k} - \frac{K_h}{\Delta z_k}\frac{\partial T}{\partial z}\bigg|_{k+1} - A_h \nabla^4 T_k, \qquad (6)$$

where $D/Dt = \partial/\partial t + \mathbf{v}_h \cdot \boldsymbol{\nabla} + w\partial/\partial z$, T_k is the temperature at the first model level (5 m), Δz_k is the thickness of the first model layer, and the other symbols have been explained in Part I. We see that there is no simple relationship between Q_T and T_k so that the EEOF approach is useful.

In a first attempt, total SST and Q_T were analyzed. Recall that this analysis allows us to find the common spatial pattern between Q_T and SST—associated with two different temporal amplitude time series, one corresponding to Q_T and the other corresponding to SST. Prior to the analyses, each time series of Q_T and SST is normalized by its own variance.

The two field ATSs associated with the first mode (accounting for 96% of the variance) are shown in Fig. 15a. Apart from the strong seasonal cycle signal characterizing both time series, we note the existence of a 2–3- (mostly 2) month lag, with the heat flux time series leading the SST. Note that this is expected if in (6) we can neglect the advective/diffusive terms. Assuming Q_T to be sinusoidal in time, we can anticipate that the SST time series will be $\pi/4$ (3 months) out of phase with respect to the Q_T time series. The fact that the time lag in our case is between 2 and 3 months can be attributed to the effects of the advective/diffusive terms and/or the vertical diffusion of heat. The spatial pattern (not shown here) corresponding to this mode involves an in-phase oscillation of the whole Mediterranean Basin.

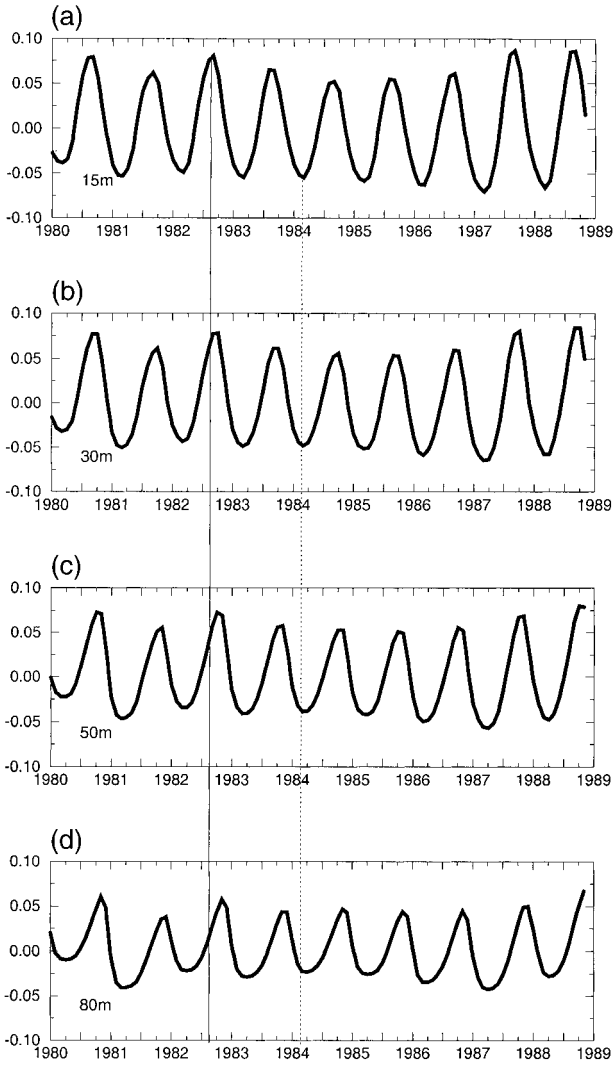

FIG. 7. The amplitude time series corresponding to the second mode at depths of 15, 30, 50, and 80 m. The two vertical lines are drawn to outline the vertical penetration of the 1982 and 1984 signals.

We now remove the overwhelming seasonal cycle from both Q_T and SST before the analyses are carried out. We also apply a 12-point low-pass Lanczos filter to each time series in order to eliminate high-frequency signals. In this case, the first mode of the EEOF accounts for 58% of the variance. The SST and Q_T amplitude time series associated with it are shown in Fig. 15b. The two time series show three distinct periods characterized by different time lags between Q_T and SST, but with Q_T always leading. The first period spans the years 1980, 1981, and 1982 where a dominant 6–7-month lag exists between the two time series. The time lag is decreased to 2 months in the second period between 1983 and the end of 1986; the lag reduces to 1–2 months from 1987 onward. Thus we can conclude that

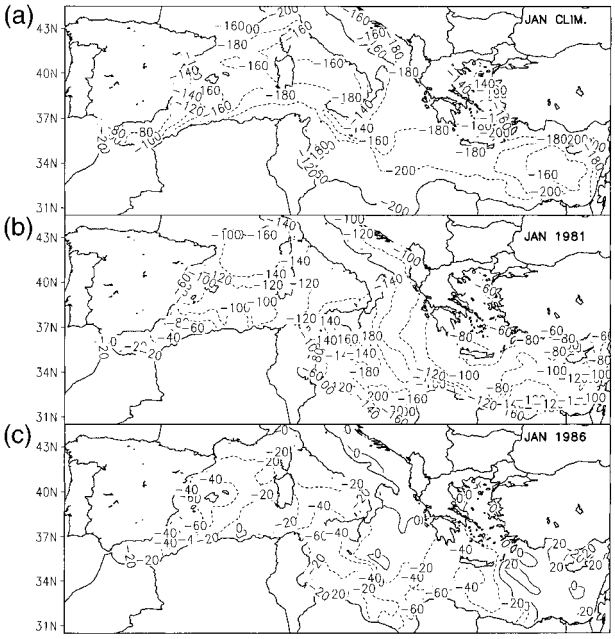

FIG. 8. (a) Jan climatology of heat flux field, and heat flux anomaly for (b) Jan 1981 and (c) Jan 1986. The units are W m^{-2}.

two anomalous periods in terms of the time lag relationship between Q_T and SST exist, corresponding to the 1980–83 and 1987–88 time frames, while the central period (1983–86) is behaving as if no major delay due to ocean dynamics occurs after Q_T is imposed (i.e., steric effect). We can argue that advection/diffusion processes

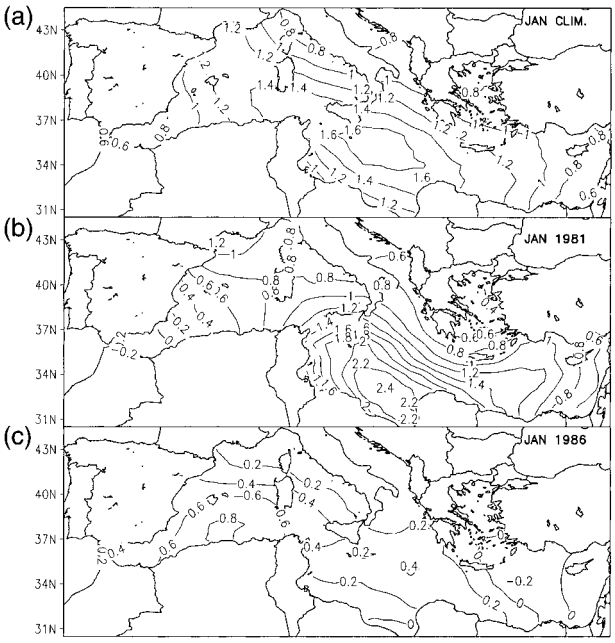

FIG. 9. (a) Jan climatology of wind stress amplitude field, and wind stress amplitude anomaly for (b) Jan 1981 and (c) Jan 1986. The units are dyn cm^{-2}.

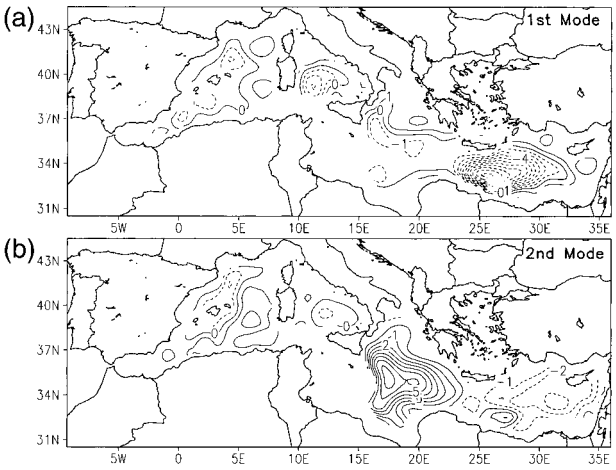

FIG. 10. The spatial patterns corresponding to the first two modes of decomposition type I applied to the anomaly dynamic height fields.

modify the ocean response to heat fluxes forcing, after large heat loss events such as the 1981 and 1987 (see Part I) winter cooling anomalies. Furthermore, we speculate that isolated severe cooling events (e.g., 1981) tend

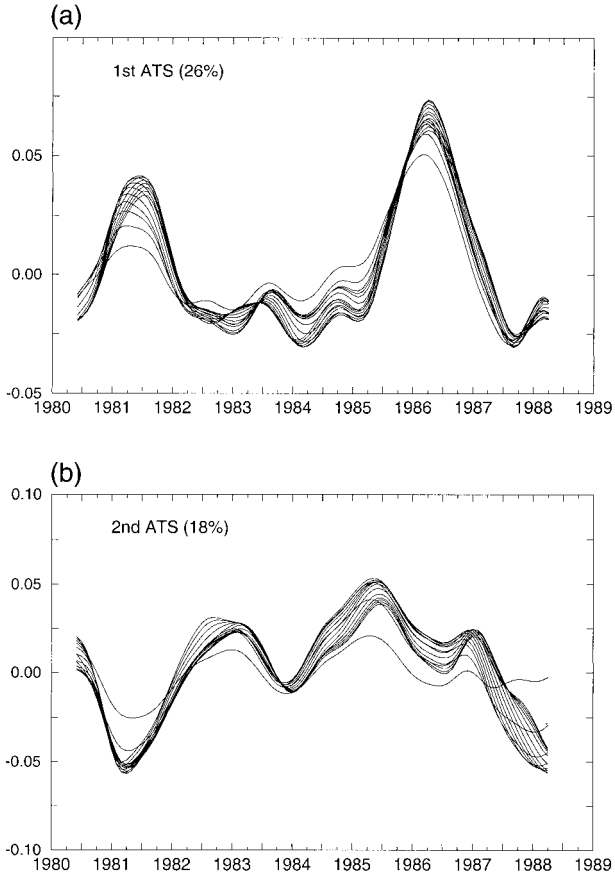

FIG. 11. The amplitude time series (for all 15 levels of analysis) corresponding to the (a) first and (b) second modes of decomposition type I applied to the anomaly dynamic height fields.

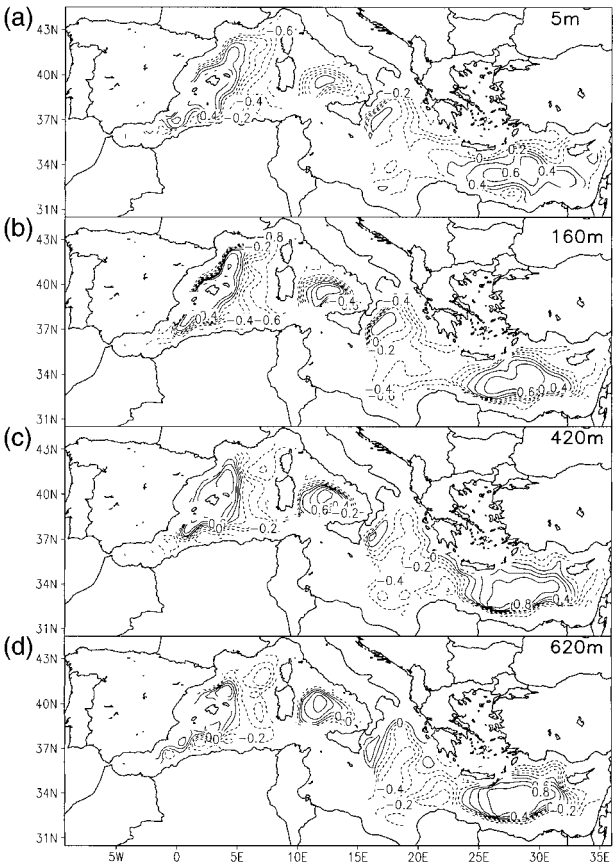

FIG. 12. The 3D EOF spatial pattern (shown at 5, 160, 420, and 620 m) corresponding to the first mode of decomposition type II applied to the anomaly dynamic height fields.

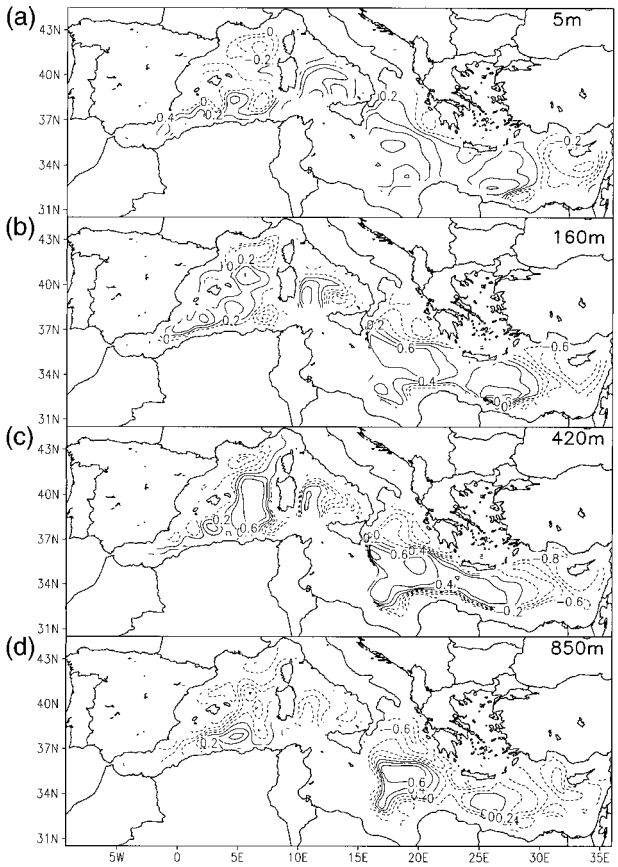

FIG. 13. The 3D EOF spatial pattern (shown at 5, 160, 420, and 850 m) corresponding to the second mode of decomposition type II applied to the anomaly dynamic height fields.

to change the phase difference between the Q_T and SST toward longer lags; that is, the ocean response to the heating cycle is delayed. On the other hand, the 1987 winter cooling event followed by large summer heating tends to reduce the phase lag between Q_T and SST to 1–2 months.

5. Summary and conclusions

In this paper we attempted a statistical analysis of the results of the central experiment presented in Part I in order to assess the temporal and spatial scales characterizing the Mediterranean general circulation variability. The statistical tools applied involve different types of EOF analyses (EOF, EEOF) applied to 2D and 3D fields, in the framework of SVD methodology.

From the 2D and 3D EOF analyses performed on the barotropic streamfunction, and the 3D anomaly dynamic height fields, respectively, we arrived at the conclusion that the barotropic and baroclinic circulation of the Mediterranean Basin are characterized by anomalous variations occurring on the subbasin gyre scales, mainly during the winter period of the years 1981 and 1986. The central Ionian and Levantine, the areas along the Spanish continental shelf, and the western coasts of Corsica–Sardinia involve the highest amplitudes of variability. The vertical structure of the anomalies is nearly uniform throughout the first kilometer of the water column.

We examined the temporal relationship characterizing the fields of sea surface temperature and total heat flux over the Mediterranean Basin, through the use of EEOF methods. On the seasonal scale, the two fields are characterized by a phase lag of 2–3 months with the total heat flux leading to the SST field. On the interannual scale, we identified the presence of two time periods where the phase lag exhibits anomalous characteristics. The first one is dominated by the strong cooling of the winter of 1981 while the second one is dominated by the strong winter cooling and summer heating events of 1987. We argue that advection/diffusion dynamics after a strong winter cooling event can change the ocean response to the subsequent heating cycle. This produces a delayed or a faster response of the ocean to external forcing. This suggests a mechanism that could account for an ocean nonlinear response to atmospheric forcing, with consequent memorization of past atmospheric events.

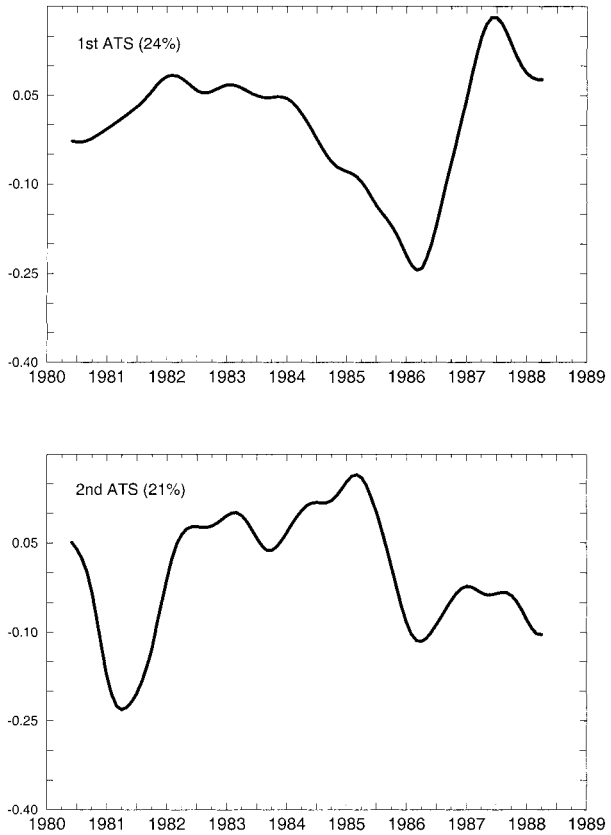

FIG. 14. The amplitude time series corresponding to the (a) first and (b) second modes of decomposition type II applied to the anomaly dynamic height fields.

Further studies are required to elucidate the dynamical response of the basin extracted from the model simulation. However, this study points out that the Mediterranean Sea general circulation has statistically significant variability at the interannual timescales on the subbasin and gyre scales. Together with the results of Part I, we can also conclude that the ocean response to wind and heat anomalies is complex and involves advection/diffusion and long memory (i.e., subduction) processes. This long memory may contribute substantially to changes in subsequent basin circulation patterns. In order to study this mechanism it is evident that longer time series of data and model simulations are needed.

Acknowledgments. This work has been supported by EU-MAST Contract MERMAIDS (MAST-CT90-0039 and MAST2-CT93-0055). The first author was supported by EU-MAST Contract B/MAST 913005. This work was finished with partial support from a MATER contract (MAS3-CT96-0051) and the MFSPP EU-MAST project (MAS3-CT98-0171). We are grateful to Dr. A. Navarra and Dr. Hans von Storch for constructive discussions and critiques of the work.

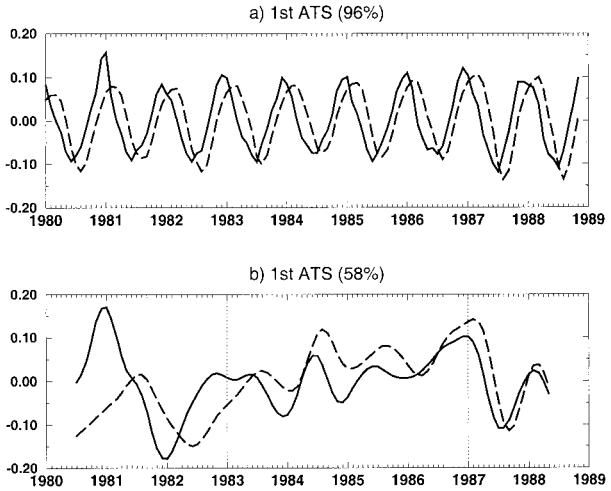

FIG. 15. Amplitude time series corresponding to the first mode of the EEOF analysis applied to the Q_t (continuous line) and SST (dashed line) fields: (a) for the total fields and (b) for the anomaly fields. The vertical lines indicate the breakdown of the time series into three distinct time periods.

APPENDIX A

EOF and SVD Methods

Consider a field (the state vector of the model for example) evolving with time. The state vector of our model is generally composed by the fields T, S, $\mathbf{v}$, ψ at each grid point of the model. For simplicity of discussion we focus on a 2D field consisting of p grid points spatially distributed. Having available n realizations of the field after a model integration, one can denote this dataset as $\mathbf{D}_{p\times n}$, where $\mathbf{D}$ is a matrix with p rows and n columns. The task of EOF analysis is to search in the p-dimensional space for the orthogonal vectors over which the scatter of the dataset is maximized while effectively reducing the dimensionality of the initial problem. In technical terms this is achieved by determining the eigenvectors of the scatter matrix

$$\mathbf{S}_{p\times p} = \mathbf{D}\mathbf{D}^{\mathrm{T}} \tag{A1}$$

($\mathbf{D}^{\mathrm{T}}$ denotes the transpose of $\mathbf{D}$ matrix). Since the $\mathbf{S}$ matrix is by construction symmetric and nonnegative definite, it has r nonnegative eigenvalues, where r is the matrix rank [$r = \min(p, n)$]. In matrix form one has to solve the eigenvalue problem

$$\mathbf{S}\mathbf{E} = \mathbf{E}\mathbf{L}, \tag{A2}$$

where $\mathbf{E}$ is the matrix of eigenvectors $e_i(x)$ ($x = 1, \ldots, p$; $i = 1, \ldots, r$) and $\mathbf{L}$ is the diagonal matrix of the eigenvalues indicated by λ_i, $i = 1, \ldots, r$. By projecting the initial dataset on the eigenvector basis one can obtain a representation of the dataset $\mathbf{D}$ in terms of $e_i(x)$ (the EOF patterns) and their amplitude coefficients $a_i(t)$ ($t = 1, \ldots, n$) called the amplitude time series:

$$\mathbf{D} = \mathbf{E}\mathbf{L}^{1/2}\mathbf{A}^{\mathrm{T}} \quad \text{or} \quad d(x, t) = \sum_{i=1}^{r} e_i(x)\lambda_i^{1/2}a_i(t). \tag{A3}$$

We should note here that the procedure can be reversed and thus solve first for the ATSs (in case $n < p$) and then project on the ATS basis to find the EOF patterns. EOF modes are usually numbered in a descending eigenvalue order so that the first mode accounts for the largest amount of total second moment (scatter or variance) of the initial dataset. The amount of total scatter accounted for by each mode is $\lambda_i/\Sigma_{i=1}^{r}\lambda_i$, where $\Sigma_{i=1}^{r}\lambda_i = \Sigma_{x=1}^{p}\Sigma_{t=1}^{n} d^2(x, t)$. The initial dataset can be efficiently represented by the first k dominant modes of the analysis (those representing most of the variance). This representation is optimal in the sense that it minimizes the quantity

$$\left\| d(x,t) - \sum_{i=1}^{k} e_i(x)\lambda_i^{1/2}a_i(t) \right\|^2 = \|d^2(x,t)\| - \sum_{i=1}^{k}\lambda_i. \quad \text{(A4)}$$

Having the first k modes representing the bulk of the second moment, a drastic reduction of the degrees of freedom of the initial dataset can be achieved and thus an economical representation.

Rules, either empirical (North 1984) or based on Monte Carlo techniques (Preisendorfer 1988), exist for deciding about the statistical significance of the modes and they will be explained in appendix B. Particular attention has to be paid to the effective number of degrees of freedom determination in cases where serial correlations exist within the data (e.g., when dealing with cyclostationary time series of data).

The singular value decomposition is a mathematical method in linear algebra (Golub and van Loan 1989) stating that any $\mathbf{D}_{p\times n}$ (singular or nonsingular) matrix of rank r can be uniquely decomposed in a matrix product of the form $\mathbf{U}\mathbf{\Sigma}\mathbf{V}^{\mathrm{T}}$, where $\mathbf{U}_{p\times r}$ is the matrix of left singular vectors, $\mathbf{\Sigma}_{r\times r}$ is the diagonal matrix of singular values, and $\mathbf{V}_{n\times r}$ is the matrix of right singular vectors. After some simple algebra, it comes out that the left singular vectors are the eigenmodes of $\mathbf{D}\mathbf{D}^{\mathrm{T}}$ scatter matrix so they are equivalent with the EOF patterns e_i, the right singular vectors are the eigenmodes of the $\mathbf{D}^{\mathrm{T}}\mathbf{D}$ scatter matrix and so are equivalent to the amplitude time series a_i, and finally the singular values are the square root of the corresponding eigenvalues of the traditional EOF analysis method. Fukumori and Wunsch (1991), Bretherton et al. (1992), and Navarra (1993) have already shown different applications of the SVD method in oceanography and meteorology. Advantages of SVD over the traditional EOF method are that it is more numerically stable (i.e., is not an eigenvalue problem) and in most cases much faster.

Having established the principles of the SVD method in the simple 2D case, we shift the discussion to the more complicated 3D case.

Let us suppose that the initial dataset consists of a three-dimensional field with p grid points at each of the m model levels with n realizations. In matrix form this set can be represented by a block matrix $\mathbf{D}_{nm\times p}$ being formed by n local matrices $\mathbf{W}_{p\times m}$:

$$\mathbf{D} = [\mathbf{W}(1)\cdots\mathbf{W}(n)]^{\mathrm{T}}, \quad \text{(A5)}$$

each representing the 3D dataset at a specific t ($t = 1, \ldots, n$). Decomposing the $\mathbf{D}$ matrix into its left and right singular vectors one achieves a representation of the form

$$d(x, z, t) = \sum_{i=1}^{r} e_i(x)\sigma_i a_i(z, t), \quad \text{(A6)}$$

where σ_i ($i = 1, \ldots, r$) are the singular values, r is the matrix rank, x runs all the grid points in the horizontal ($x = 1, \ldots, p$), z runs the m levels and $t = 1, \ldots, n$. We call (A6) decomposition type I.

The percentage of total scatter accounted for by the ith mode is simply $\sigma_i^2/\Sigma_{j=1}^{r}\sigma_j^2$. In the same way the fraction of scatter accounted for by this mode at level k (z_k) is given by the formula

$$s_i(z_k) = 1 - \frac{\sum_x \sum_t [d(x, z_k, t) - e_i(x)\sigma_i a_i(z_k, t)]^2}{\sum_x \sum_t d^2(x, z_k, t)}. \quad \text{(A7)}$$

The representation of the initial dataset as a sum of products of time and depth invariant horizontal patterns $e_i(x)$ with the temporal varying modulation coefficients $a_i(z, t)$ is not the only one possible. Indeed we can have a representation of the form

$$d(x, z, t) = \sum_{i=1}^{r'} e_i'(x, z)\sigma_i' a_i'(t) \quad \text{(A8)}$$

if the SVD decomposition is applied to the block matrix $\mathbf{D}_{n\times m\cdot p}$, which is composed of m local matrices $\mathbf{Q}_{n\times p}$:

$$\mathbf{D} = [\mathbf{Q}(1)\cdots\mathbf{Q}(n)]^{\mathrm{T}}. \quad \text{(A9)}$$

In this case the left singular vectors of matrix $\mathbf{D}_{n\times m\cdot p}$ are the depth-invariant temporal modulation coefficients of the three-dimensional EOF patterns.

We call (A8) decomposition type II. In both decomposition types I and II we call, for convenience, the part that is time dependent ATS, no matter if it is depth invariant or not.

We should say here that in the problem formulation there is an open issue concerning separability and what is achievable statistically might not be necessarily physically correct. Moreover the orthogonality property that the EOF analysis poses to the different modes may not have a physical counterpart. Indeed, as one can argue in most cases, physical processes are interrelated and not orthogonal to each other. Thus the analysis offers only a better understanding of the temporal–spatial scales of the system variability along with a much more economical representation. Decomposition type I, which involves an expansion of the initial four-dimensional field into depth-invariant structures [e.g., (A6)], allows for a better study of the temporal behavior at each separate depth in distinction to decomposition type II of

3D EOF analysis that intermixes the temporal behavior of different depths.

If the analysis dataset consists of heterogeneous fields varying in time, for example, atmospheric forcing fields and ocean dynamical fields, we can use an analysis tool called extended EOF. To retain the formalism as in (A6) or (A8), m can denote a number of different 2D fields. The EEOFs are amenable to decomposition types I or II. In our applications we have used decomposition type I in order to study the temporal relationship between the model SST and total heat flux fields.

APPENDIX B

Testing the Statistical Significance of the EOF Modes

We present here a worked-out example in testing the significance of the various 2D EOF modes. The technique used has been put forward by Preisdendorfer (1988) as a selection rule named rule N and involves the estimation of the 95% and 5% significance levels for each of the EOF modes. The null hypothesis to be tested is that the $p \times n$ (where p stands for the number of spatial points and n for the sample size) dataset has been drawn randomly from a normally distributed population of zero mean in the p-dimensional space. It is implicitly assumed that the dataset examined is normally distributed, thus its robustness is not guaranteed in cases of highly nonnormal distributions. A point to be mentioned is that the statistical test considers only the eigenvalues of the dataset scatter matrix and not the information given by the corresponding temporal or spatial patterns. Details for the technique can be found in Preisendorfer (1988).

Our application involves the EOF analysis performed on the total barotropic streamfunction fields of the model integration. The dataset in this case consists of $p = 3085$ spatial points while the length of each time series is $n = 107$ (sample size). In Fig. A1b the continuous line shows the normalized eigenvalue curve,

$$\frac{\lambda_i}{(n-1)^{-1}\sum_{k=1}^{n-1}\lambda_k} \qquad i = 1, \ldots, 26,$$

of the dataset for the first 26 modes, along with the 95% and 5% significance levels (dotted lines) as estimated by rule N, which almost coincides due to the very small ratio n/p. Following the test, the null hypothesis is rejected for the first 11 modes while for the rest of the modes it is accepted. However, in cases of strong month to month correlations (serial correlation), the initial sample size has to be further decreased to the so called effective sample size n^*. An average value of 0.76 for 1-month lag correlation existing in our dataset gives an effective sample size of $n^* = 28$. Application of rule N in this case leads to the rejection of the null hypothesis for the first six modes and the acceptance for the rest of the modes (results for this case are shown in Fig. A1a). Thus, the reduction of the sample size due to the strong serial correlation existing in dataset affects the statistical significance of the modes and leads to the acceptance of a smaller number of modes as compared to the case where the effect of the 1-month lag correlations are not taken into consideration.

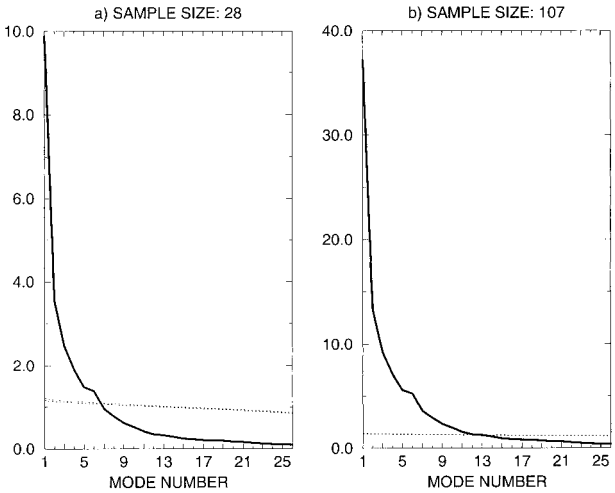

FIG. A1. (a) Normalized curve of the first 26 eigenvalues (continuous line) of the 2D EOF analysis applied on the total barotropic streamfunction field along with the 95% and 5% significance levels (dotted lines) for $n^* = 28$; (b) as in (a) but for the case of $n = 107$.

REFERENCES

Bretherton, C. S., C. Smith, and J. M. Wallace, 1992: An intercomparison of methods for finding coupled patterns in climate data. *J. Climate,* **5,** 541–560.

Fukumori, I., and C. Wunsch, 1991: Efficient representation of the North Atlantic hydrographic and chemical distributions. *Progress in Oceanography,* Vol. 27, Pergamon Press, 111–195.

Golub, G. H., and C. F. van Loan, 1989: *Matrix Computation.* Johns Hopkins University Press, 642 pp.

Korres, G., N. Pinardi, and A. Lascaratos, 2000: The ocean response to low-frequency interannual atmospheric variability in the Mediterranean Sea. Part I: Sensitivity experiments and energy analysis. *J. Climate,* **13,** 705–731.

Lorenz, E. N., 1956: Empirical orthogonal functions and statistical weather prediction. Statistical Forecast Project Tech. Rep. 1, Dept. of Meteorology, Massachusetts Institute of Technology, 49 pp. [Available from MIT, 77 Massachusetts Ave., Cambridge, MA 02139.]

Navarra, A., 1993: A new system of orthonormal modes for linearized meteorological application. *J. Atmos. Sci.,* **50,** 16, 2569–2583.

North, G. R., 1984: Empirical orthogonal functions and normal modes. *J. Atmos. Sci.,* **41,** 879–887.

Preisendorfer, R. W., 1988: *Principal Component Analysis in Meteorology and Oceanography.* Elsevier Science, 425 pp.

——, F. W. Zwiers, and T. P. Barnett, 1981: Foundations of principal component selection rules. Scripps Institute of Oceanography Ref. Series 81–4, 192 pp. [NTIS PB83–146613.]

Wallace, J., C. Smith, and C. S. Bretherton, 1991: Singular value decomposition of wintertime sea surface temperature and 500-mb height anomalies. *J. Climate,* **5,** 561–576.